analytical chemistry

pubs.acs.org/ac Article

CoID-LAMP: Color-Encoded, Intelligent Digital LAMP for Multiplex Nucleic Acid Quantification

Kai Wu,[§] Qi Fang,[§] Zhantao Zhao, and Zida Li*

Cite This: https://doi.org/10.1021/acs.analchem.2c05665 Read Online

ACCESS | Metrics & More | Article Recommendations | Supporting Information

ABSTRACT: Multiplex, digital nucleic acid tests have important biomedical applications, but existing methods mostly use fluorescent probes that are target-specific and difficult to optimize, limiting their widespread applications. Here, we report color-encoded, intelligent digital loop-mediated isothermal amplification (CoID-LAMP) for the coidentification of multiple nucleic acid targets. CoID-LAMP supplements different primer solutions with different dyes, generates primer droplets and sample droplets, and collectively pairs these two types of droplets in a microwell array device to perform LAMP. After imaging, the droplet colors were analyzed to decode the primer information, and the precipitate byproducts within droplets were detected to determine the target occupancy and calculate the concentrations. We first established an image analysis pipeline based on a deep learning algorithm for reliable droplet detection and validated the analytical performance in nucleic acid quantification. We then implemented CoID-LAMP using fluorescent dyes as the coding materials and established an 8-plex digital nucleic acid assay, confirming the reliable coding performance and the capability of multiplex nucleic acid quantification. We further implemented CoID-LAMP using brightfield dyes for a 4-plex assay, suggesting that the assay could be realized solely by brightfield imaging with minimal demand on the optics. Leveraging the advantages of droplet microfluidics in multiplexing and deep learning in intelligent image analysis, CoID-LAMP offers a useful tool for multiplex nucleic acid quantification.

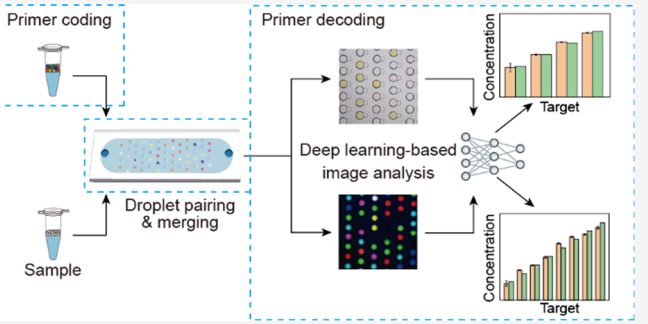

INTRODUCTION

Nucleic acid tests provide important information for the identification of pathogen infections,[1−4] assessment of cancer risks,[5,6] and planning of personalized treatment.[7] In addition, simultaneous testing of multiple nucleic acid targets enables fast, accurate, and economical diagnostics. For example, in the care of pathogen infection, timely identification of the specific types of pathogens can support the decisions on treatment plans and transmission prevention.[8]

Nucleic acid tests have been predominantly achieved by nucleic acid amplification tests, such as real-time polymerase chain reaction (qPCR). However, qPCR and alike rely on standard samples for references, giving a relative quantification of nucleic acids. To achieve absolute quantification, digital PCR (dPCR) emerged. dPCR compartmentalizes the reaction mix into discrete chambers and performs amplification therein. By examining the amplification readout of each compartment, the nucleic acid concentration can be inferred, thus eliminating the need of external references.

To achieve simultaneous detection of multiple nucleic acid targets in dPCR, it is necessary to identify the specific targets encapsulated in each compartment. This goal is mostly achieved by designing fluorescent probes with different emitting wavelengths. Therefore, by examining the fluorescent color of each droplet, the encapsulated targets can be detected. For example, in the detection of SARS-CoV-2 virus, TaqMan probes targeting ORF1ab, N, and RNase P Genes were labeled with the fluorescent dyes of FAM, HEX, and Cy5, respectively, enabling the simultaneous detection of these three genes.[9] In addition to fluorescence wavelength, stratified fluorescence intensity has been utilized to expand the multiplexity. By designing different amplicon lengths, primer concentrations,[10] and probe concentrations[11−13] for different targets, the droplets containing different targets emit different intensities of fluorescence. Consequently, the encapsulated targets in each compartment can be identified based on the relative fluorescence intensity. Moreover, melting temperature can serve as a signature of nucleic acid targets and was utilized as an additional dimension to achieve multiplexing.[5,14,15] Despite the demonstrated success, these strategies are compromised by the fluctuation in the generated fluorescence intensity, insufficient fluorescence

Received: December 19, 2022
Accepted: March 3, 2023

channels, expensive optics and reagents, and laborious protocol optimization.

Another strategy is to encode each experiment condition when simultaneously performing multiple amplification reactions and subsequently decode each experiment.[16] For example, microbeads with different fluorescences were conjugated with different primers, thus offering a means to recover the primer information based on the detected fluorescence of the beads.[17] However, the microbead-based multiplexing strictly required droplet encapsulation of single beads, which complicated the sample preparation steps of the assay. Microwell array in conjunction with droplet color coding of the Cas13 detection reagents was proposed to achieve multiplex detection.[18,19] Despite the massive multiplexity this method has enabled, it required off-chip pre-amplification of the sample, making it less compatible with digital quantification.

Nucleic acid tests with absolute quantification, high multiplexity, easy operation, and low instrument cost are yet to be developed. To address that, here we report color-encoded, intelligent digital loop-mediated isothermal amplification (CoID-LAMP), which coidentifies multiple nucleic acid targets using digital LAMP in conjunction with droplet color coding and intelligent image analysis. CoID-LAMP encodes droplets of primers with dyes and collectively pairs these droplets with sample droplets containing nucleic acid targets of interest on a microwell array device. After merging and amplification, the occupancy of each droplet is detected by analyzing the precipitated byproduct of the amplification under brightfield imaging, and the encapsulated primer is recovered by decoding the color of the droplet. We first developed an image analysis pipeline using the deep learning algorithm of YOLOv5 for droplet segmentation and identification and validated the analytical performance of this method. The results showed a limit of blank of 18.1 copies/μL and a dynamic range from 1.27 $\times$ 10^2 to 1.27 $\times$ 10^4 copies/μL. We then implemented CoID-LAMP using fluorescent dyes as the coding materials and established an 8-plex digital nucleic acid assay, confirming the reliable coding performance and the capability of multiplex nucleic acid quantification. We further implemented CoID-LAMP using brightfield dyes and achieved similar performance, suggesting that CoID-LAMP could be implemented solely using brightfield imaging with minimal demand on the optics. Leveraging the advantages of droplet microfluidics in multiplexing and deep learning in intelligent image analysis, CoID-LAMP represents a great technology for multiplex nucleic acid quantification.

METHODS

Device Fabrication. Three microfluidic devices were used, including a droplet generator to make large (primer) droplets, a droplet generator to make small (sample) droplets, and a microwell array to pair these two types of droplets. Droplet generators were fabricated using replica molding of poly(dimethylsiloxane) (PDMS, Sylgard 184, Dow). The silicon mold used SU-8 as the structure, and the mold fabrication was outsourced to a microfabrication facility (Suzhou Research Materials Microtech Company, China) following standard photolithography protocols. The SU-8 molds were oxygen plasma-treated (PDC-002, Harrick Plasma) for 1 min and silanized in a vacuum chamber for 6 h. PDMS prepolymers with a 10:1 base-to-hardener ratio was then poured on the SU-8 molds and cured at 60 °C for 10 h, before being peeled off, cut into desired shapes, and punched to generate inlets and outlets with diameters of 1.1 mm. The PDMS slab and a plain glass slide (10127101-G, Citotest Labware) were then treated with oxygen plasma for 1 min, placed in contact, and baked at 110 °C for 10 min to complete bonding. The devices were then baked at 60 °C for at least 24 h to turn the microchannels hydrophobic.

The microwell array device was fabricated following the steps described in Figure S1 to ensure minimal droplet evaporation during amplification. Briefly, glass slides were drilled to generate holes with diameters of 3 mm, and the holes were then filled with PDMS prepolymer and cured. Meanwhile, an SU-8 mold was fabricated using dual-layer photolithography, with the bottom and top layer being 50 and 20 μm, respectively. Consequently, the large microwell (Φ90 μm) and the small microwell (Φ50 μm) had a depth of 70 and 50 μm, respectively. PDMS molds were generated by replica molding with reverse images of the final microwells, i.e., micropillars, were silanized and applied with a thin layer of PDMS prepolymer. The glass slides were then plasma-treated and placed on top of the PDMS molds, before being degassed and cured. The glass slides were subsequently peeled off from the molds, resulting in a thin layer of (~150 μm) of PDMS with microwell structures bonded on the glass slide backing. Inlets and outlets with diameters of 1.1 mm were then punched on the PDMS hole-filler. A spacing layer was fabricated by laser cutting the laminated film composed of a layer of double-sided tape (9448A, 3M Company) and a layer of Parafilm (PM996, Bemis Company). Finally, the glass slide with microwell features, a spacing layer, and a plain glass slide were assembled using a device clamp (WH-CF-04, Wenhao Co., China). The region with the microwell arrays was 40 mm × 18 mm, housing roughly 23,000 microwell units.

Reagents. Eight commercial, proprietary LAMP kits were used, which targeted *Listeria monocytogenes* (011061M), *Staphylococcus aureus* (011071M), *Aeromonas hydrophila* (012051MIII), *Aeromonas sobria* (012061M), *Bacillus subtilis* (011131M), *Legionella pneumophila* (012011M), *Bacillus cereus* (011221M), and *Shigella* (011041M). All kits were purchased from Guangzhou Double Helix Gene Technology Co. The specificity was confirmed by performing cross-reactivity tests using a real-time PCR instrument (QuantStudio 1, Thermo Fisher Scientific; data not shown). The concentrations of the positive controls were quantified by performing droplet digital LAMP, with droplet diameters being around 90 μm (~0.382 nL). Droplets were collected in 0.2 mL PCR tubes (PCR-0208-C and PCR-2CP-RT-C, Axygen) and amplified at 63 °C for 45 min in a thermal cycler (TOM300, Shanghai Tomos Science). The droplet generation oil used a commercial droplet digital PCR oil (1864006, Bio-Rad Laboratories, Inc.). Three fluorescent dyes (K1068R-AF405, K0068R-AF488, K1068R-AF594, SolarBio Life Sciences) with excitation wavelengths of 405, 488, and 594 nm, respectively, were used. All were diluted to 20 μg/mL in the working conditions. In addition, three brightfield dyes (red and blue: 052100053080, McCormick & Company, Inc.; orange: Orange G, O100205, Shanghai Aladdin Biochemical Technology Co.) were used.

Experiment Setup. The primer droplets and sample droplets were generated using two different flow-focusing microfluidic devices (Figure S2) by infusing the oil and aqueous phase into the devices using syringe pumps (LSP01-2A, Longer Pump), glass syringes (1 mL, Shanghai Bolige), and tubing (BB31695-PE/2, Scientific Commodities Inc.). The flow rates of the oil and aqueous phase were 300 and 500 μL/h, respectively, to generate the primer droplets and 800 and 500

https://doi.org/10.1021/acs.analchem.2c05665
Anal. Chem. XXXX, XXX, XXX−XXX

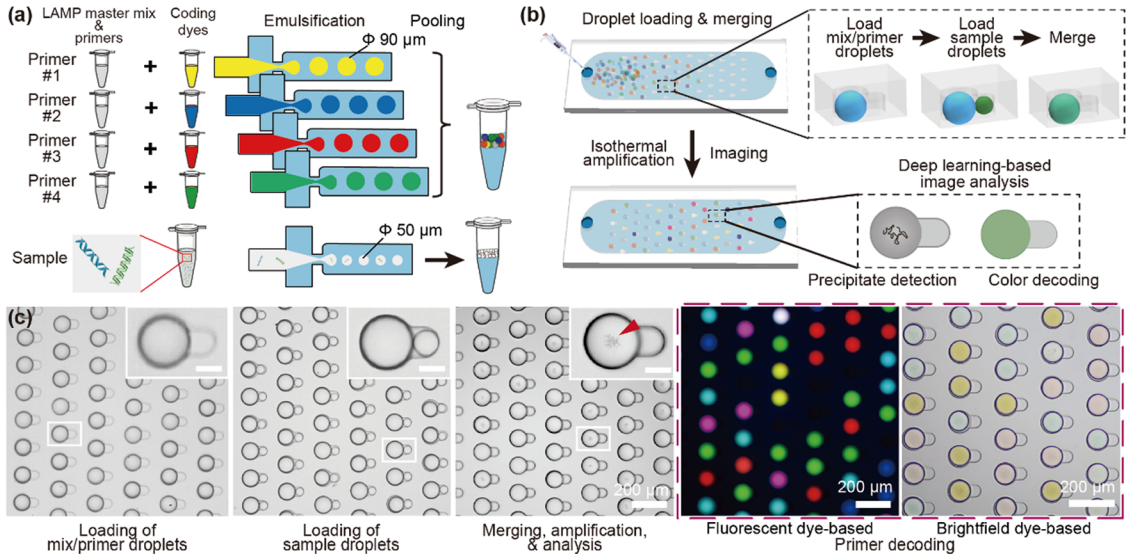

Figure 1. Overview of the color-encoded, intelligent digital LAMP (CoID-LAMP). (a) Schematic showing the preparation of color-coded primer droplets and sample droplets. Primer droplets had a larger diameter. (b) Schematic showing the sequential loading, merging, amplification, and imaging of the droplets. The precipitate byproducts were used as the indicator of positive droplets. (c) Micrographs showing the different steps of the droplet operation. Either the fluorescent dye or the brightfield dye can be used for color coding. The red arrow indicates the generated precipitates. Scale bars in insets: 50 μm.

μL/h, respectively, to generate the sample droplets. Due to the small volume of the aqueous solution, the syringe and tubing were prefilled with oil (Novec 7500, 3M) before drawing up the aqueous solution into the tubing. A pipette tip was connected to the outlet to collect the generated droplets. The hands-on operation, including tubing connecting and sample loading, took roughly 5 min, and the droplet generation took roughly 5 min. The generated droplets could be stored at 4 °C for at least 5 days without obvious coalescence. The large droplets, which contained the primer and master mix, were loaded into the microwell array device using a micropipette, before the small droplets, which contained the sample, were loaded in the same manner. The two types of droplets were merged by moving a corona treater (BD-20AC, Electro-Technic Products) on the top of the device back and forth for about 5 s. The device was then incubated at 63 °C for 60 min for LAMP. The device was then imaged using an inverted microscope (Eclipse Ti2-E, Nikon) coupled with an automated stage and cameras (DS-Qi2, Nikon; SC-2000, iMG).

Data Analysis. The image analysis pipeline used YOLOv5 as the main algorithm.[20] The algorithm used the PyTorch framework, and the backbone model used the CSP-Darknet53. The default nonmaximum suppression threshold of 0.25 was adopted. There were three detection layers, and each detection layer had three anchor boxes, with the dimensions being 10 × 13, 16 × 30, 23 × 33, 30 × 61, 45 × 62, 59 × 119, 90 × 1440, 156 × 198, and 326 × 373 in pixels. The strides were 8, 16, and 32 pixels. The training data were labeled in LabelImg based on the visual inspection of the presence of precipitates.[21] Thirty images were labeled in total, resulting in roughly 1500 droplets (300 positives and 1200 negatives), and the training and test sets were randomly split at a ratio of 2:1. The original images were scaled from 1608 × 1608 pixels to 640 × 640 pixels to accelerate the training. During the training, the default hyperparameters for low-augmentation COCO training from scratch were used. In particular, the optimization adopted stochastic gradient descent algorithm with an initial learning rate of 0.01 and final learning rate of 0.0001. The data augmentation measures include (1) augmentation on the color HSV of the images, (2) random image transformation, namely, 10% translation, 50% resizing, and 50% probability of horizontal flipping, and (3) mosaic data augmentation. The models were trained up to 400 epochs on a GPU (GeForce RTX 3080 Ti, Nvidia Corporation). During detection, target objects were confined to those with the aspect ratio between 0.85 and 1.5 and both dimensions larger than 90 pixels.

To decode the fluorescence colors, the fluorescence images were first automatically thresholded to binary images based on the grayscale distribution. The bounding boxes of each droplet obtained from the analysis of the brightfield image were then used to locate the corresponding droplet in the binarized fluorescence images. The total number of the TRUE pixels within the bounding box in the binarized fluorescence images was used to judge the presence of the fluorescence, and the threshold of the pixel numbers was set as 2500 pixels. To decode the brightfield colors, the bounding box of each droplet was first obtained as aforementioned, and the bounding box was scaled down to half from the box center to include only the droplet. The RGB values within the bounding box were averaged, and a few conditions were manually prescribed to determine the color based on the average RGB values. The judging conditions were shown in the flowchart shown in Figure S8. The detected primer and occupancy data were then used to calculate nucleic acid concentrations following the equation $C = -\ln P/V$, where P is the fraction of the negative droplets and V is the volume of the small (sample) droplets. Each experiment was performed with at least three replicates to assess the means and standard deviations. The limit of blank (LoB) was obtained by measuring blank samples and calculated following the equation $\text{LoB} = \text{mean}_{\text{blank}} + 1.645 \times \text{SD}_{\text{blank}}$.[22] The dynamic range was calculated as the range of concentrations where the R^2 was larger than 0.98 after linear fitting.

RESULTS

Overview of CoID-LAMP. To achieve simultaneous, absolute quantification of multiple nucleic acid targets, CoID-

https://doi.org/10.1021/acs.analchem.2c05665
Anal. Chem. XXXX, XXX, XXX−XXX

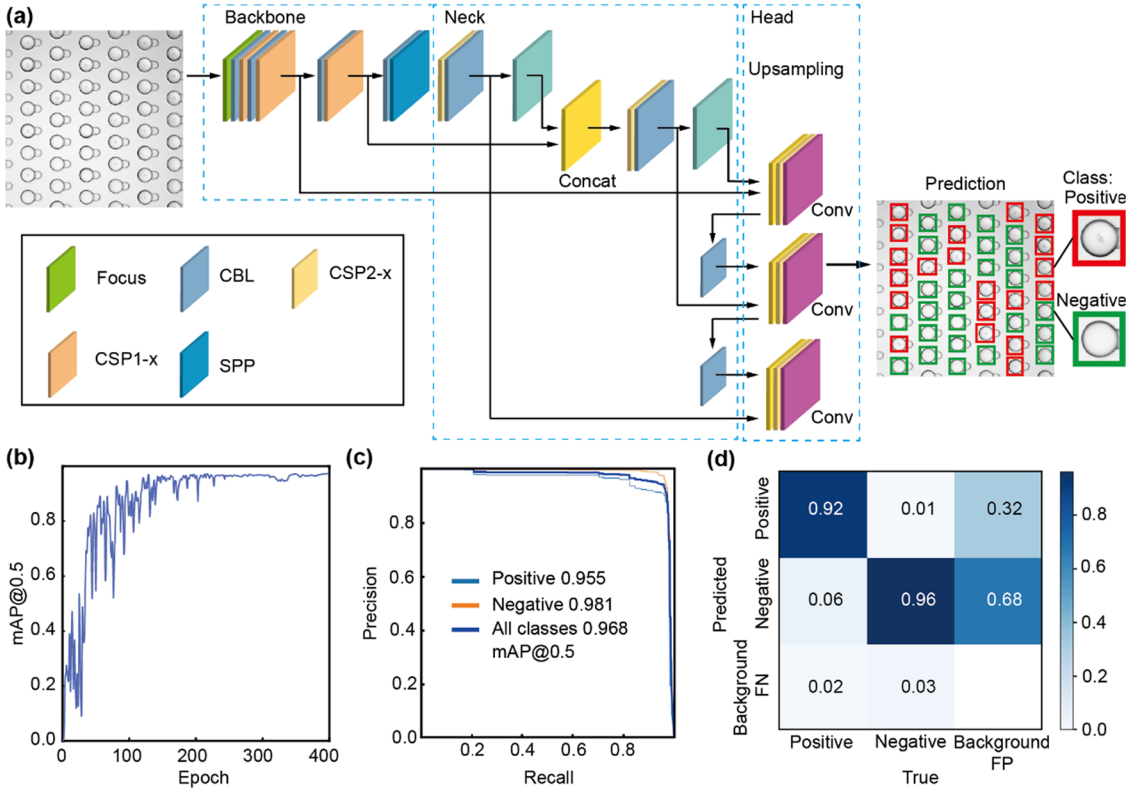

Figure 2. Schematic showing the deep learning-based image analysis pipeline and the performance. (a) Architecture of the YOLOv5 algorithm implemented for the object detection of positive and negative droplet in CoID-LAMP. The Focus layer slices the original image and concatenates the slices. CBL stands for Convolution, Batch Normalization, and Leaky ReLU activation function. CSP1-*x* and CSP2-*x* were based on the Cross Stage Partial Networks with different parameters of CBL components and residual units. SPP stands for spatial pyramid pooling and is used to pool and concatenate the multiscale region features. (b) Mean Average Precision (mAP) as a function of epochs. (c) Precision−recall curve of the positive, negative, and all classes at 400 epochs and the corresponding mAP@0.5. (d) Confusion matrix showing the accuracy of the trained model. FP, false positive. FN, false negative.

LAMP uses dyes to encode primers designed for the amplification of different targets and a microwell array device to pair the pooled primer droplets with the sample droplets. After LAMP, the droplets are imaged to analyze the droplet colors, decode the encapsulated primers, and detect the amplification product, generating data for the absolute quantification of each nucleic acid target of interest. Specifically, primers, along with the master mix, are supplemented with dyes and emulsified to generate color-encoded primer droplets, as shown in Figure 1a. The sample was also emulsified into droplets but with a smaller size using a different droplet generator (Figure S1). The primer droplets had a diameter of 88.6 ± 1.7 μm, and the sample droplets had a diameter of 49.9 ± 1.4 μm. The primer droplets could be stored at 4 °C for at least 5 days without obvious coalescence (Figure S2). A microwell array device was used for droplet pairing and merging, as previously described.[23] Each microwell unit was composed of a large well (Φ90 μm) and a small well (Φ50 μm) that were interconnected, and the depths were 70 and 50 μm, respectively. As shown in Figure 1b,c and Video S1, primer droplets (~Φ90 μm) were first loaded into the microwell array device and occupied the large well of each microwell unit. Sample droplets (~Φ50 μm) were subsequently loaded into the device and occupied the small wells. The paired primer and sample droplets were then merged by destabilizing the interface using corona treatment, completing the mixing between the sample and different primers. The device was then incubated at 63 °C to perform LAMP, generating precipitates of magnesium pyrophosphate in droplets where the encapsulated target matched with the primer.[24−26] The droplets were then imaged on-chip to determine the target occupancy by detecting the presence of the precipitate and decode the encapsulated primer by detecting the droplet color, and the data were then used to quantify the concentrations of each target (see the Methods Section). The assay turnaround time was about 2 h, including 10 min for sample droplet generation, 15 min for sample droplet loading, 60 min for amplification, 20 min for chip imaging, and 10 min for data analysis.

CoID-LAMP performs on-chip amplification, where droplet evaporation has been a common issue due to the gas permeability of PDMS.[27] To address that, we engineered a PDMS−glass hybrid microfluidic chip, which used glass as the substrate and a thin layer of PDMS to house the microwell array, thus minimizing the presence of PDMS in the device (Figure S3). Compared to the all-PDMS device, this hybrid device significantly reduced droplet evaporation and bubble formation during incubation, and droplets retained more than 95% of the original volume throughout the assay (Figure S4). In addition, the droplet manipulation was optimized to ensure that more than 99% of the droplets were successfully merged (Figure S5).

Deep Learning-Based Image Analysis Pipeline. We then sought to develop an image analysis pipeline, which automatically detects each droplet in the brightfield images and classifies the droplets based on the presence of precipitates. We implemented the YOLOv5 algorithm, which is a deep learning algorithm designed for object detection with superior robustness over the conventional morphological image analysis.[20] In our

https://doi.org/10.1021/acs.analchem.2c05665
Anal. Chem. XXXX, XXX, XXX−XXX

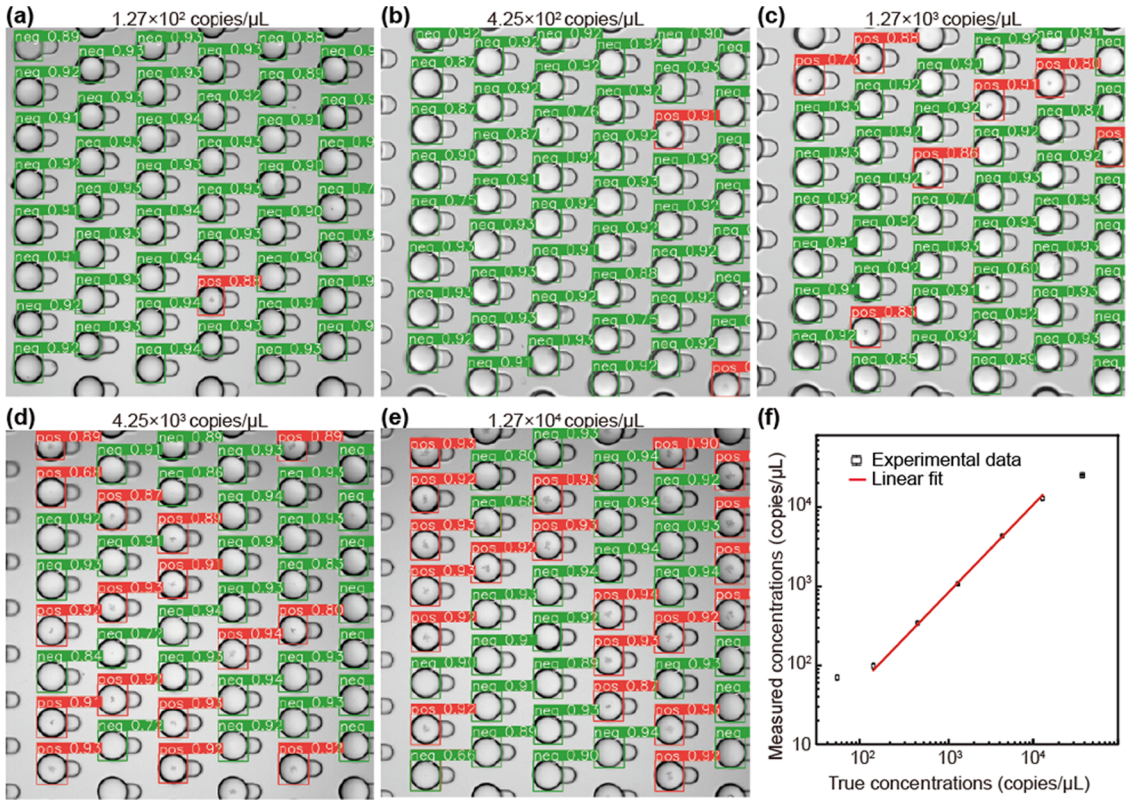

Figure 3. Characterization of the performance of CoID-LAMP in nucleic acid quantification. (a−e) Micrographs with detected positive and negative droplets boxed in red and green and labeled as "pos" and "neg," respectively, using samples of different concentrations as indicated. The numbers represent the scores of the detected objects, and thresholds of 0.75 were set for both classes of objects. (f) Measured nucleic acid concentrations of samples with different known concentrations. Data represent mean ± S.D. with $n = 3$.

case, the algorithm aimed to detect two types of objects within each image, namely, positive droplets and negative droplets. The implemented algorithm used Focus and CSP-Darknet as the Backbone Layer, FPN and PAN as the Neck Layer, and CIOU-Loss as the loss function of the bounding box on the Head Layer, as shown in Figure 2a. The original image was first fed into the Focus layer, which sliced the original image into four slices, concatenated the slices in depth, and passed it to a convolutional layer. After that, the image went through a few basic components of the network, including CBL, CSP1-*x*, CSP2-*x*, and SPP. The CBL component consisted of the Convolution, Batch Normalization, and Leaky ReLU activation functions. The CSP1-*x* component was based upon the Cross Stage Partial Networks with *x* times of Res units. The CSP2-*x* component was also based upon the Cross Stage Partial Networks, with *x* times of CBL modules. SPP stands for spatial pyramid pooling, and it is used to pool and concatenate the multiscale region features. The data set was generated by labeling droplets with precipitates as "positive" and without precipitates as "negative". Thirty images were labeled, generating roughly 300 droplet objects with "positive" labels and 1200 droplet objects with "negative" labels. The training and test data were split at the ratio of 2:1. The model showed good performance on the experimental data. As shown in Figure 2b, the mean Average Precision at the Intersection over Union (IoU) threshold of 0.5 (mAP@0.5) tended to stabilize at around 0.95 after 250 epochs in the training. At the epochs of 400, the prediction of both the positives and negatives obtained good accuracy, as shown by the precision−recall curve in Figure 2c. The mAP@0.5 of the positives, negatives, and all classes was 0.955, 0.981, and 0.968, respectively. We further examined the performance of object detection in a confusion matrix. As shown in Figure 2d, 0.92 of the true positive droplets and 0.96 of the true negative droplets were successfully detected. In addition, only 2% of the true positive droplets and 3% of the true negative droplets were not detected, as indicated by the Predicted Background False Negative (FN) in Figure 2d. Furthermore, droplets that were inaccurately detected from the background objects were very rare compared to the overall droplets (Background False Positive, FP). These results suggested that the detection was adequately accurate. In addition, on the current hardware, the processing of each image (640 × 640 × 3 pixels) took 43.2 ms. In a typical experiment, the data could be processed in 4 min including writing of the labeled images.

Characterization of the Quantification Capability. With the image analysis pipeline established, we then sought to characterize the analytical performance of the CoID-LAMP as a digital nucleic acid amplification test. We used samples of a single nucleic acid target with known concentrations, namely, 1.27×10^2, 4.25×10^2, 1.27×10^3, 4.25×10^3, and 1.27×10^4 copies/μL, and performed droplet digital LAMP on the microwell array device. We followed the protocol of CoID-LAMP as afore-described except that only one type of primer droplets was used. Primer droplets and sample droplets were sequentially loaded into the microwell array device, merged, incubated for amplification, and imaged. The image analysis pipeline was then applied to the images to calculate the nucleic acid concentrations based on Poisson distribution. Since it was the sample droplets that carried the nucleic acid targets and each sample droplets had a diameter of 50 μm, equivalent to the

https://doi.org/10.1021/acs.analchem.2c05665
Anal. Chem. XXXX, XXX, XXX−XXX

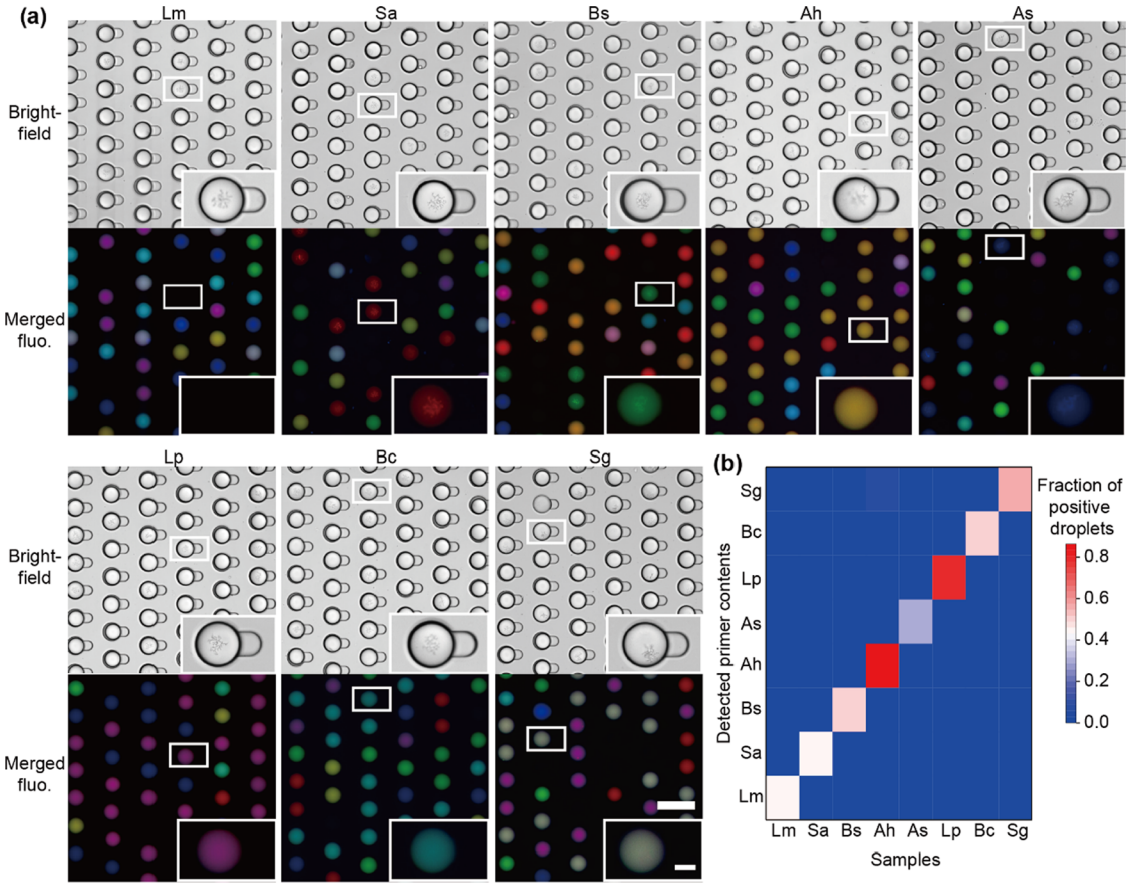

Figure 4. Color coding of primer information using fluorescent dyes. (a) Brightfield and merged fluorescence micrographs of the droplets after amplifications. The primer droplets were the pool of eight types of color-coded primer droplets, and the sample droplets were generated using samples containing single types of targets, as indicated. Due to Poisson distribution, only a fraction of the sample droplets contained the targets. Precipitates were only detected in droplets with the matching color (primers). Scale bars: 200 μm in the main figures and 50 μm in the insets. (b) Fraction of positive droplets among each type of primer contents when testing samples with different single targets.

volume of 0.065 nL, the volume value was set at 0.065 nL for the concentration calculation. The algorithm successfully detected and classified the droplets, and as the concentration increased, a larger fraction of positive droplets was present, as boxed in red by the algorithm in Figure 3a–e. The measured concentration showed good agreement with the true concentrations (Figure 3f). For example, when the sample concentration was 1.27×10^2, 1.27×10^3, and 1.27×10^4 copies/μL, the fractions of positive droplets were 0.65 ± 0.05, 6.84 ± 0.10, and 57.50 ± 1.73%, respectively, and the measured concentrations were $(1.00 \pm 0.10) \times 10^2$, $(1.07 \pm 0.02) \times 10^3$, and $(1.32 \pm 0.08) \times 10^4$ copies/μL, respectively. The R^2 was 0.9986 after linear fitting, indicating that the dynamic range covered 1.27×10^2–1.27×10^4 copies/μL. We additionally performed experiments to characterize the limit of blank by testing blank samples three times. The results showed that the limit of blank was 18.1 copies/μL. False positives (~0.086%) were detected when testing blank samples, and it was likely induced by the debris on the device that appeared in the background of the negative droplets, resulting in the relatively inconsistent detection performance of blank samples.

Fluorescent Dye-Based Color Coding. With the image analysis pipeline established and the quantification capability validated, we then sought to implement the color-coding strategy of the CoID-LAMP. Fluorescent dyes are commonly used in biomedical applications with easy access. Therefore, we first chose fluorescent dyes to prove the concept. We selected fluorescent dyes of three colors, namely, blue (405 nm), green (488 nm), and red (594 nm), which enabled eight color codes by setting each color on or off (Table S1). The dyes were supplemented into the primer/master mixes based on the coding plan (Figure 1a). After amplification, both brightfield and fluorescence micrographs were collected. The image analysis pipeline detected droplets in the brightfield images, and the fluorescence signals of each droplet were extracted from the fluorescence images to recover the primer information (Figure S6a). High-temperature incubation during the amplification could potentially compromise the stability of the fluorophores and induce bleaching. We specifically tested the effect of incubation on the fluorescence intensity of the dyes of choice, and the results showed that the bleaching effect was negligible (Figure S6b). Consequently, the extracted colors could be easily classified based on the intensity of the three fluorescent colors (Figure S6c).

To validate that the fluorescent colors could be correctly decoded to recover the primer information, we performed the fluorescent dye-based CoID-LAMP on samples containing a single type of known nucleic acid targets. We chose eight types of bacteria, namely, *Listeria monocytogenes* (Lm), *Staphylococcus aureus* (Sa), *Aeromonas hydrophila* (Ah), *Aeromonas sobria* (As), *Bacillus subtilis* (Bs), *Legionella pneumophila* (Lp), *Bacillus cereus* (Bc), and *Shigella* (Sg), as the detection targets and used the

https://doi.org/10.1021/acs.analchem.2c05665
Anal. Chem. XXXX, XXX, XXX−XXX

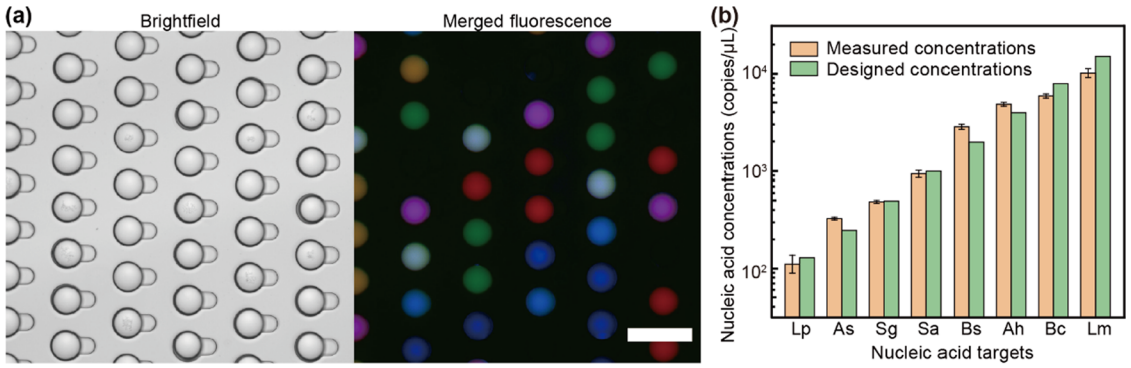

Figure 5. Simultaneous detection of eight types of nucleic acids using fluorescent dye-based CoID-LAMP. (a) Brightfield and merged fluorescence micrographs of the droplets after amplification. Scale bar: 200 μm. (b) Measured nucleic acid concentrations of each target in comparison with the known values. Data represent mean ± S.D. with n = 3.

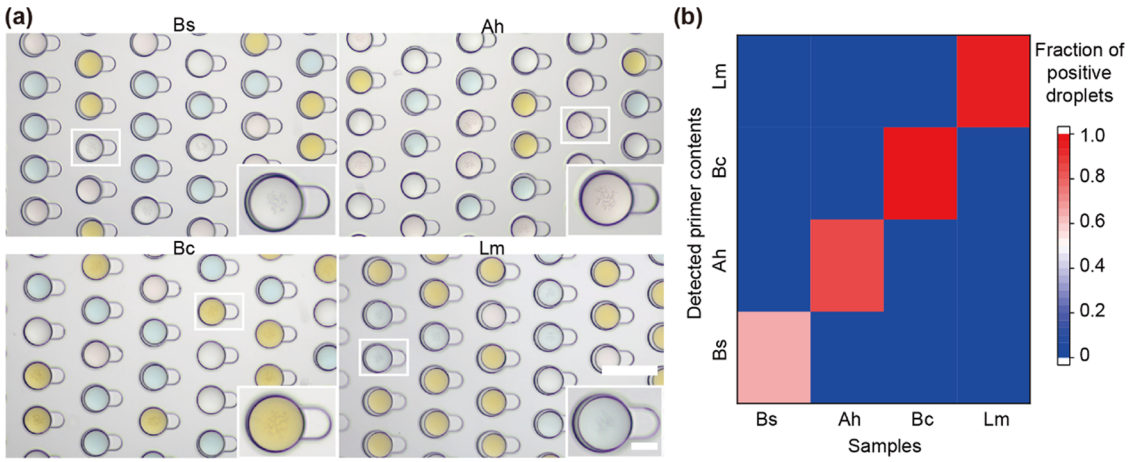

Figure 6. Color coding of primer information using brightfield dyes. (a) Brightfield micrographs of the droplets after amplifications. The primer droplets were the pool of four types of color-coded primer droplets, and the sample droplets contained only a single type of target, as indicated. Precipitates were only detected in droplets with the matching color (primers). Scale bars: 200 μm in the main figures and 50 μm in the insets. (b) Fraction of positive droplets among each type of primer contents when testing samples with different single targets.

corresponding LAMP primers with demonstrated specificity.[28] The eight sets of primers were coded with fluorescent dyes and encapsulated in droplets along with the master mix, before being pooled and loaded into the microwell array device. Eight samples, each containing one of the eight nucleic acids, were emulsified into droplets and loaded into the microwell array device in eight separate experiments. The process of the sample emulsification followed Poisson distribution, and only a fraction of the sample droplets contained the targets. After amplification, the droplets were imaged and analyzed. The results showed that, in each experiment, precipitates were detected only in the droplets with the correct color code, as shown in Figure 4a. For example, the primer droplets containing Bs primers were coded in green fluorescence. In the test of the sample containing Sa nucleic acids, positive droplets were only detected in droplets emitting red fluorescence, accounting for 49.1% of these droplets. In contrast, among droplets emitting other combinations of fluorescence, almost no positive droplets were observed, with the fraction of positive droplets being 0.1, 0, 0, 0.1, 0, 0, and 0% for droplets of other seven colors, as shown in Figure 4b. These results suggested that the primer information could be correctly decoded based on the droplet color using fluorescent dyes.

We then performed multiplex nucleic acid quantification using fluorescence-based CoID-LAMP by testing samples containing the mixture of these eight types of targets with designated concentrations. In the experiments, roughly 1200 brightfield images were captured, resulting in about 60,000 droplets. The images were processed using the trained YOLOv5 model to output the occupancy and location of each droplet, and the location was then used to query the primer information from the fluorescence images. The primer and occupancy data were then consolidated to quantify the concentration of each nucleic acid target based on Poisson distribution. We intentionally designed the sample with target concentrations spanning the dynamic range. As shown in Figures 5 and S6d, the fluorescence-based CoID-LAMP successfully amplified the targets and detected the primers using the fluorescence signals. The quantified results also agreed with the known values. For example, the designed concentrations for Lp, Sg, Sa, and Ah were 130, 500, 1000, and 4000 copies/μL, and the measured concentrations were 118 ± 29, 498 ± 11, 950 ± 98, and 4823 ± 190 copies/μL, respectively. These results demonstrated the validity of using fluorescent dyes as the color-coding materials for the implementation of CoID-LAMP.

Brightfield Dye-Based Color Coding. We then aimed to explore the possibility of using brightfield dyes in lieu of fluorescent dyes for the color coding in CoID-LAMP. With brightfield dyes, the imaging step could be completed by capturing solely the brightfield channel, which would simplify

https://doi.org/10.1021/acs.analchem.2c05665
Anal. Chem. XXXX, XXX, XXX−XXX

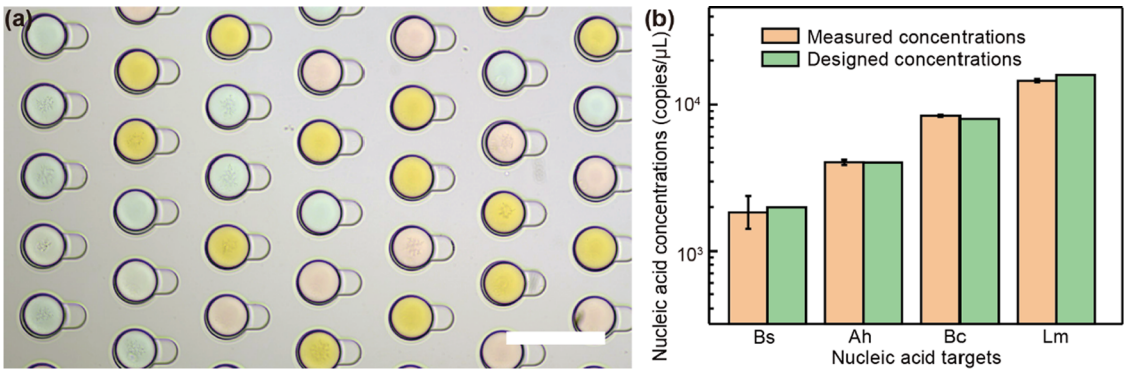

Figure 7. Simultaneous detection of four types of nucleic acids using brightfield dye-based CoID-LAMP. (a) Brightfield micrographs of the droplets after amplification. Scale bar: 200 μm. (b) Measured nucleic acid concentrations of each target in comparison with the known values. Data represent mean ± S.D. with n = 3.

the data acquisition, eliminate the demand of fluorescence optics, and significantly reduce the instrument cost. The dyes were supplemented into the primer/master mixes to complete the color coding, and the CoID-LAMP protocols were then followed to generate brightfield images of the droplets and analyze the presence of the precipitates. In addition, the RGB values of each droplet were analyzed to recover the primer content within each droplet.

To ensure that the selected dyes did not affect the amplification, we first performed experiments to determine the proper concentrations for each dye with detectable colors in brightfield but negligible influence on the amplification. Three types of dye conditions were successfully identified for color coding (Figure S7). Droplets with no dyes were used as the fourth color code. The average RGB values of blank, red, blue, and green droplets are (217, 216, 208), (215, 195, 194), (249, 224, 82), and (183, 202, 201), respectively. The four colors showed little overlap in the RGB space (Figure S8), suggesting that these four colors could be differentiated with proper judging conditions. We then used these three dyes to implement the color coding of CoID-LAMP and performed the entire experiment. The results showed that the droplets, though with colors, could still be successfully detected by the trained image analysis model. We designed a simple algorithm to classify and decode the color based on the RGB values (Figure S9). As shown in Figure S10, the colors of the droplets were correctly identified by the program. To further validate the color-coding strategy, we tested samples containing single types of targets, namely, Bs, Ah, Bc, and Lm nucleic acids, while using the pooled primer droplets for these four types of targets. Indeed, the results showed that only droplets with correct colors had precipitates (Figure 6a). For example, when testing the sample containing Ah nucleic acid, only droplets with pink color, which were designed to code the Ah primer droplet, had precipitates. The quantified results further confirmed this observation. As shown in Figure 6b, almost no positive droplets were observed when the color or the primer content did not match the target in the samples. For example, when testing the sample containing the Bs target, positive droplets among the droplets with decoded primers of Bs, Ah, Bc, and Lm accounted for 50.8, 0.2, 0, and 0%, respectively. These results confirmed that the color-coding strategy could indeed be reliably implemented using brightfield dyes for the CoID-LAMP.

We further performed multiplex nucleic acid quantification using the brightfield dye-based CoID-LAMP by testing samples containing a mixture of these four types of nucleic acid targets with designed concentrations. The acquired brightfield images were then used to detect the occupancy as well as the primer content of the droplets using the image analysis pipeline. Results showed that the color of the droplets could be easily distinguished in brightfield, and precipitates were observed in a fraction of the droplets (Figures 7a and S11). The data of the recovered primer information and the detected occupancy were used to calculate the nucleic acid concentrations of each target. The results showed good agreement with the designed concentrations (Figure 7b). For example, the measured concentrations of Bs, Ah, Bc, and Lm were 1883 ± 454, 4018 ± 168, 8389 ± 144, and 14601 ± 406 copies/μL, which were close to the designed values of 2000, 4000, 8000, and 16,000 copies/μL, respectively. These results confirmed the feasibility of CoID-LAMP using brightfield dyes as the color-coding materials.

CONCLUSIONS

In this work, we developed a digital, multiplex nucleic acid assay, named CoID-LAMP, for the coidentification of multiple nucleic acid targets. CoID-LAMP uses dyes to color-code the primers within each droplet and deep learning image analysis to detect the droplets and recover the primer information. We first developed an image analysis pipeline, validated its accuracy, and then characterized the analytical performance of CoID-LAMP in absolute quantification of nucleic acids. We then demonstrated the feasibility of CoID-LAMP using common fluorescent dyes as the color-coding materials. We further implemented CoID-LAMP using brightfield dyes and proved its validity, indicating that CoID-LAMP could be implemented by brightfield imaging. The high multiplexity, low-cost, and low demand on instrumentation make CoID-LAMP a useful tool for nucleic acid tests.

Due to the interference of dye molecules on the polymerase reaction, currently we have only established three available brightfield dyes and achieved a 4-plex nucleic acid test. To further increase the multiplexity, future work could be devoted to systematically investigating the effect of dyes on amplification and discovering more amplification-friendly dyes. In addition, instead of using soluble dyes, colored microbeads could be used as an alternative coding material since it imposes little influence on the reagent system. Combinations of microbeads with different colors can be spiked into the primer solutions before droplet generation, and the primer information can be recovered by detecting the presence of microbeads within each droplet (Figure S12). Future work could also be devoted to exploring

https://doi.org/10.1021/acs.analchem.2c05665
Anal. Chem. XXXX, XXX, XXX−XXX

the opportunity of using colored bead-based droplet coding for multiplex assays. Furthermore, the current work proved the concept of CoID-LAMP using standard samples. The assay could be further validated using clinical samples in future work.

■ ASSOCIATED CONTENT

Supporting Information

The Supporting Information is available free of charge at https://pubs.acs.org/doi/10.1021/acs.analchem.2c05665.

Additional experimental details, including figures of device designs and fabrication; experimental data on droplet evaporation, droplet merging, and color analysis; and a video showing the droplet operation (PDF)

Video showing the capturing of large and small droplets and the merging process (MP4)

■ AUTHOR INFORMATION

Corresponding Author

Zida Li − *Department of Biomedical Engineering, Medical School, Shenzhen University, Shenzhen 518060, China; Guangdong Key Laboratory for Biomedical Measurements and Ultrasound Imaging, Department of Biomedical Engineering, Medical School, Shenzhen University, Shenzhen 518060, China;* orcid.org/0000-0002-1353-9414; Email: zidali@szu.edu.cn

Authors

Kai Wu − *Department of Biomedical Engineering, Medical School, Shenzhen University, Shenzhen 518060, China; Guangdong Key Laboratory for Biomedical Measurements and Ultrasound Imaging, Department of Biomedical Engineering, Medical School, Shenzhen University, Shenzhen 518060, China*

Qi Fang − *Department of Biomedical Engineering, Medical School, Shenzhen University, Shenzhen 518060, China; Guangdong Key Laboratory for Biomedical Measurements and Ultrasound Imaging, Department of Biomedical Engineering, Medical School, Shenzhen University, Shenzhen 518060, China*

Zhantao Zhao − *Department of Biomedical Engineering, Medical School, Shenzhen University, Shenzhen 518060, China; Guangdong Key Laboratory for Biomedical Measurements and Ultrasound Imaging, Department of Biomedical Engineering, Medical School, Shenzhen University, Shenzhen 518060, China*

Complete contact information is available at: https://pubs.acs.org/10.1021/acs.analchem.2c05665

Author Contributions

§K.W. and Q.F. contributed equally to this work. K. W. and Z.L. conceptualized the project and designed the experiments. K.W. and Q.F. performed the experiments. Q.F. and Z.Z. wrote the image analysis program. K.W., Q.F., and Z.Z. analyzed the data. K.W., Q.F., and Z.L. wrote the manuscript. All authors commented on the manuscript.

Notes

The authors declare no competing financial interest.

■ ACKNOWLEDGMENTS

This work was supported by the Natural Science Foundation of Guangdong Province (2019A1515012010), Shenzhen Overseas Talent Program, and Shenzhen University Student Research Grants (8672206-000001).

■ REFERENCES

(1) Chapman, S. J.; Hill, A. V. *Nat. Rev. Genet.* **2012**, *13*, 175−188.

(2) Churchill, M. J.; Deeks, S. G.; Margolis, D. M.; Siliciano, R. F.; Swanstrom, R. *Nat. Rev. Microbiol.* **2016**, *14*, 55−60.

(3) Grubaugh, N. D.; Ladner, J. T.; Lemey, P.; Pybus, O. G.; Rambaut, A.; Holmes, E. C.; Andersen, K. G. *Nat. Microbiol.* **2019**, *4*, 10−19.

(4) Han, Q.; Lin, Q.; Jin, S.; You, L. *J. Infect.* **2020**, *80*, 373−377.

(5) Nakagawa, T.; Tanaka, J.; Harada, K.; Shiratori, A.; Shimazaki, Y.; Yokoi, T.; Uematsu, C.; Kohara, Y. *Anal. Chem.* **2020**, *92*, 11705−11713.

(6) Bournet, B.; Muscari, F.; Buscail, C.; Assenat, E.; Barthet, M.; Hammel, P.; Selves, J.; Guimbaud, R.; Cordelier, P.; Buscail, L. *Clin. Transl. Gastroenterol.* **2016**, *7*, No. e157.

(7) Takai, E.; Totoki, Y.; Nakamura, H.; Morizane, C.; Nara, S.; Hama, N.; Suzuki, M.; Furukawa, E.; Kato, M.; Hayashi, H.; Kohno, T.; Ueno, H.; Shimada, K.; Okusaka, T.; Nakagama, H.; Shibata, T.; Yachida, S. *Sci. Rep.* **2015**, *5*, No. 18425.

(8) Chen, L.; Zhang, G.; Liu, L.; Li, Z. *Talanta* **2021**, *225*, No. 121986.

(9) Yin, H.; Wu, Z.; Shi, N.; Qi, Y.; Jian, X.; Zhou, L.; Tong, Y.; Cheng, Z.; Zhao, J.; Mao, H. *Biosens. Bioelectron.* **2021**, *188*, No. 113282.

(10) McDermott, G. P.; Do, D.; Litterst, C. M.; Maar, D.; Hindson, C. M.; Steenblock, E. R.; Legler, T. C.; Jouvenot, Y.; Marrs, S. H.; Bemis, A.; Shah, P.; Wong, J.; Wang, S.; Sally, D.; Javier, L.; Dinio, T.; Han, C.; Brackbill, T. P.; Hodges, S. P.; Ling, Y.; Klitgord, N.; Carman, G. J.; Berman, J. R.; Koehler, R. T.; Hiddessen, A. L.; Walse, P.; Bousse, L.; Tzonev, S.; Hefner, E.; Hindson, B. J.; Cauly, T. H., III; Hamby, K.; Patel, V. P.; Regan, J. F.; Wyatt, P. W.; Karlin-Neumann, G. A.; Stumbo, D. P.; Lowe, A. J. *Anal. Chem.* **2013**, *85*, 11619−11627.

(11) Chen, W.; Zheng, J.; Wu, C.; Liu, S.; Chen, Y.; Liu, X.; Du, J.; Wang, J. *Clin. Chem.* **2019**, *65*, 1051−1059.

(12) Liu, C.; Li, B.; Lin, H.; Yang, C.; Guo, J.; Cui, B.; Pan, W.; Feng, J.; Luo, T.; Chu, F.; Xu, X.; Zheng, L.; Yao, S. *Biosens. Bioelectron.* **2021**, *194*, No. 113615.

(13) Zhang, Y.; Zhang, P.; Chen, L.; Kaushik, A.; Hu, K.; Wang, T.-H. *Biosens. Bioelectron.* **2020**, *167*, No. 112499.

(14) Athamanolap, P.; Hsieh, K.; O'Keefe, C. M.; Zhang, Y.; Yang, S.; Wang, T.-H. *Anal. Chem.* **2019**, *91*, 12784−12792.

(15) Velez, D. O.; Mack, H.; Jupe, J.; Hawker, S.; Kulkarni, N.; Hedayatnia, B.; Zhang, Y.; Lawrence, S.; Fraley, S. I. *Sci. Rep.* **2017**, *7*, No. 42326.

(16) Duncombe, T. A.; Dittrich, P. S. *Curr. Opin. Biotechnol.* **2019**, *60*, 205−212.

(17) Xu, W.; Chen, C.; Ma, X.; Yuan, L.; Liu, S.; Zheng, K.; Li, J. *Chem. Commun.* **2017**, *53*, 5866−5869.

(18) Ackerman, C. M.; Myhrvold, C.; Thakku, S. G.; Freije, C. A.; Metsky, H. C.; Yang, D. K.; Ye, S. H.; Boehm, C. K.; Kosoko-Thoroddsen, T.-S. F.; Kehe, J.; Nguyen, T. G.; Carter, A.; Kulesa, A.; Barnes, J. R.; Dugan, V. G.; Hung, D. T.; Blainey, P. C.; Sabeti, P. C. *Nature* **2020**, *582*, 277−282.

(19) Welch, N. L.; Zhu, M.; Hua, C.; Weller, J.; Mirhashemi, M. E.; Nguyen, T. G.; Mantena, S.; Bauer, M. R.; Shaw, B. M.; Ackerman, C. M.; Thakku, S. G.; Tse, M. W.; Kehe, J.; Uwera, M.-M.; Eversley, J. S.; Bielwaski, D. A.; McGrath, G.; Braidt, J.; Johnson, J.; Cerrato, F.; Moreno, G. K.; Krasilnikova, L. A.; Petros, B. A.; Gionet, G. L.; King, E.; Huard, R. C.; Jalbert, S. K.; Cleary, M. L.; Fitzgerald, N. A.; Gabriel, S. B.; Gallagher, G. R.; Smole, S. C.; Madoff, L. C.; Brown, C. M.; Keller, M. W.; Wilson, M. M.; Kirby, M. K.; Barnes, J. R.; Park, D. J.; Siddle, K. J.; Happi, C. T.; Hung, D. T.; Springer, M.; MacInnis, B. L.; Lemieux, J. E.; Rosenberg, E.; Branda, J. A.; Blainey, P. C.; Sabeti, P. C.; Myhrvold, C. *Nat. Med.* **2022**, *28*, 1083−1094.

(20) Jocher, G.YOLOv5 by Ultralytics *Git code*, 2020 https://github.com/ultralytics/yolov5.

(21) Tzutalin, LabelImg *Git code*, 2015 https://github.com/tzutalin/labelImg.

(22) Armbruster, D. A.; Pry, T. *Clin. Biochem. Rev.* **2008**, *29*, S49−S52.

https://doi.org/10.1021/acs.analchem.2c05665
Anal. Chem. XXXX, XXX, XXX−XXX

(23) Xie, R.; Liu, Y.; Wang, S.; Shi, X.; Zhao, Z.; Liu, L.; Liu, Y.; Li, Z. *Biosens. Bioelectron.* **2023**, *220*, No. 114913.
(24) Muñoz, H. E.; Riche, C. T.; Kong, J. E.; van Zee, M.; Garner, O. B.; Ozcan, A.; Di Carlo, D. *ACS Sens.* **2020**, *5*, 385−394.
(25) Chen, L.; Ding, J.; Yuan, H.; Chen, C.; Li, Z. *Adv. Sci.* **2022**, *9*, No. 2105450.
(26) Mori, Y.; Nagamine, K.; Tomita, N.; Notomi, T. *Biochem. Biophys. Res. Commun.* **2001**, *289*, 150−154.
(27) Kopp, M. R. G.; Linsenmeier, M.; Hettich, B.; Prantl, S.; Stavrakis, S.; Leroux, J.-C.; Arosio, P. *Anal. Chem.* **2020**, *92*, 5803−5812.
(28) Yuan, H.; Chao, Y.; Li, S.; Tang, M. Y. H.; Huang, Y.; Che, Y.; Wong, A. S. T.; Zhang, T.; Shum, H. C. *Anal. Chem.* **2018**, *90*, 13173−13177.

https://doi.org/10.1021/acs.analchem.2c05665
Anal. Chem. XXXX, XXX, XXX−XXX